**Weierstraß-Institut**

**für Angewandte Analysis und Stochastik**

**Leibniz-Institut im Forschungsverbund Berlin e. V.**

# Multiband $\mathrm{k} \cdot \mathrm{p}$ model and fitting scheme for *ab initio*-based electronic structure parameters for wurtzite GaAs

Oliver Marquardt[1], Miguel A. Caro[2,3], Thomas Koprucki[1],

Peter Mathé[1], Morten Willatzen[4,5]

submitted: March 5, 2020

[1] Weierstraß-Institut
Mohrenstr. 39
10117 Berlin, Germany
E-Mail: oliver.marquardt@wias-berlin.de
thomas.koprucki@wias-berlin.de
peter.mathe@wias-berlin.de

[2] Department of Electrical
Engineering and Automation
Aalto University
02150 Espoo, Finland

[3] Department of Applied Physics
Aalto University
02150 Espoo, Finland

[4] Technical University of Denmark
Department of Photonics Engineering
DK-2800 Kongens Lyngby, Denmark

[5] Beijing Institute of Nanoenergy and Nanosystems
Chinese Academy of Sciences
Beijing, China

No. 2699

Berlin 2020

# Multiband $\mathbf{k} \cdot \mathbf{p}$ model and fitting scheme for *ab initio*-based electronic structure parameters for wurtzite GaAs

Oliver Marquardt, Miguel A. Caro, Thomas Koprucki,
Peter Mathé, Morten Willatzen

**Abstract**

We develop a 16-band $\mathbf{k} \cdot \mathbf{p}$ model for the description of wurtzite GaAs, together with a novel scheme to determine electronic structure parameters for multiband $\mathbf{k} \cdot \mathbf{p}$ models. Our approach uses low-discrepancy sequences to fit $\mathbf{k} \cdot \mathbf{p}$ band structures beyond the eight-band scheme to most recent *ab initio* data, obtained within the framework for hybrid-functional density functional theory with a screened-exchange hybrid functional. We report structural parameters, elastic constants, band structures along high-symmetry lines, and deformation potentials at the $\Gamma$ point. Based on this, we compute the bulk electronic properties ($\Gamma$ point energies, effective masses, Luttinger-like parameters, and optical matrix parameters) for a ten-band and a sixteen-band $\mathbf{k} \cdot \mathbf{p}$ model for wurtzite GaAs. Our fitting scheme can assign priorities to both selected bands and $\mathbf{k}$ points that are of particular interest for specific applications. Finally, ellipticity conditions can be taken into account within our fitting scheme in order to make the resulting parameter sets robust against spurious solutions.

## 1    Introduction

The development of novel electronic devices and light sources requires efficient techniques to model the optoelectronic properties of semiconductor nanostructures. For about two decades now, the six- and eight-band $\mathbf{k} \cdot \mathbf{p}$ formalisms represent the backbone of semiconductor device modelling and have been extensively employed to study semiconductor nanostructures of a wide range of shapes, dimensions, and material compositions. [1, 14, 39, 21, 31, 20] These approaches describe the bulk electronic band structure of a material perturbatively, such that it is well reproduced in the vicinity of a selected high-symmetry point within the Brillouin zone (BZ), commonly the zone center $\Gamma$. For the description of heterostructures consisting of different materials or crystal phases, the $\mathbf{k} \cdot \mathbf{p}$ formalism is employed within envelope functions that contain the description of the shape and dimensions of the heterostructure in a continuum picture. An accurate description of the electronic properties of semiconductor nanostructures using $\mathbf{k} \cdot \mathbf{p}$ models can be achieved only if the electronic properties are governed by the band structure around the high-symmetry point selected for the corresponding $\mathbf{k} \cdot \mathbf{p}$ model. The small number of relevant electronic structure parameters required for these well-established $\mathbf{k} \cdot \mathbf{p}$ models: band offsets, energy splittings, electron- and hole effective masses (the latter are commonly translated to Luttinger-like parameters), deformation potentials and optical matrix elements, are widely available for most III-V [37, 36, 30] and many II-VI compound semiconductors. [38, 16]

On the other hand, the eight-band $\mathbf{k} \cdot \mathbf{p}$ model has shortcomings that, despite its past and recent successes, make it unsuited for a number of material systems and devices: The limitation of the set of basis functions to the top three valence bands and the bottom conduction band with their respective $|\uparrow\rangle$ and $|\downarrow\rangle$ components makes this model a priori unsuited to materials such as GaSb or GaAs in the

wurtzite (WZ) phase, where an additional conduction band plays a decisive role. [22] The perturbative approach yields a good description of the electronic band structure around the BZ center, $\mathbf{k} = \mathbf{0}$, whereas the limitation to one conduction band and three valence bands coupled via optical matrix elements cannot resolve all features of the band structure throughout the BZ, so that the description of indirect band gap materials such as Si or Ge, where the minimum of the conduction band is not at the same $\mathbf{k}$ value as the maximum of the valence band, requires a larger basis, e.g., a 15-band or even 30-band $\mathbf{k} \cdot \mathbf{p}$ model. [6, 27]

The existing parameter sets, for instance compiled in the remarkable work by Vurgaftman and coworkers [37] and its update for the III-N semiconductors [36], that provide all essential parameters for most compound semiconductors, are limited to the eight-band model. Furthermore, the application of the eight-band $\mathbf{k} \cdot \mathbf{p}$ formalism and envelope function approach to heterostructures can – under some conditions – find erroneous, so-called spurious solutions that result from a loss of ellipticity of the respective $\mathbf{k} \cdot \mathbf{p}$ Hamiltonian operator. [33] While existing parameter sets have been evaluated for selected semiconductor materials, [33, 34, 35] ellipticity conditions have, to our knowledge, never been taken into account directly in the calculation of $\mathbf{k} \cdot \mathbf{p}$ electronic structure parameter sets.

The scope of our work is to provide a versatile tool that can generate parameter sets for $\mathbf{k} \cdot \mathbf{p}$ models of arbitrary complexity and level of sophistication including, but also going beyond, six or eight basis functions. We focus on WZ GaAs, as this material can be employed in novel nanowire-based crystal-phase heterostructures [11] and the description of its electronic structure requires the consideration of at least one additional conduction band. [22, 12]

We derive a sixteen-band $\mathbf{k} \cdot \mathbf{p}$ Hamiltonian that takes the second relevant conduction band close to the band gap as well as the following three conduction bands into account, to provide a better accuracy and validity of the whole band structure throughout wide parts of the BZ.

We compute the corresponding 16-band $\mathbf{k} \cdot \mathbf{p}$ parameter set by fitting the $\mathbf{k} \cdot \mathbf{p}$ band structure to an up-to-date *ab initio* band structure.

We note that the parameter fitting tool presented is suited to other materials such that it can be employed to provide a full spectrum of up-to-date $\mathbf{k} \cdot \mathbf{p}$ parameters of III-V and II-VI semiconductor materials as well as of any material of which the band structure can be described using a parameterized Hamiltonian, independent of the existence of a band gap. Our approach enables us to increase the fitting priority of selected bands and high-symmetry-points within the BZ in order to produce the best-suited set of parameters for applications that rely on the correct description of these bands and high-symmetry-points. Furthermore, our tool facilitates the calculation of $\mathbf{k} \cdot \mathbf{p}$ parameter sets that avoid spurious solutions in the simulation of the electronic properties of nanostructures as it allows us to control the non-ellipticity of the Hamiltonian operator matrix to a certain extent.

## 2   Band structure calculation

In order to obtain up-to-date band structure parameters for multi-band $\mathbf{k} \cdot \mathbf{p}$ models, we have carried out hybrid-functional density functional theory (DFT) calculations of the electronic properties of GaAs in the WZ phase (For details, see Appendix A).

Equilibrium lattice parameters and WZ internal parameter were obtained by fitting the total energy of the crystal to an equation of state. The elastic constants were computed from the stress tensor, rather than total energy derivatives, which allows for more accurate results. [7] The structural parameters and elastic constants obtained are listed in Table 2. Note that the internal WZ parameter $u$ is lower than

Table 1: Structural and elastic parameters for ZB and WZ GaAs. Experimental values, where available, are in brackets. a: Ref. [37], b: Ref. [23]

|  | ZB GaAs | WZ GaAs |
|---|---|---|
| $a$ (Å) | 5.671 (5.642[a]) | 3.997 (3.989[b]) |
| $c$ (Å) | n/a | 6.588 (6.564[b]) |
| $u$ | n/a | 0.3741 |
| $C_{11}$ (GPa) | 119 | 142 |
| $C_{12}$ (GPa) | 51 | 46 |
| $C_{13}$ (GPa) | n/a | 28 |
| $C_{33}$ (GPa) | n/a | 167 |
| $C_{44}$ (GPa) | 80 | 40 |

Table 2: Band gaps, position of the topmost valence band with respect to the average electrostatic potential, SO splittings and CF splittings of WZ GaAs obtained with SO coupling enabled.

| | |
|---|---|
| $E_{\mathrm{g}}$ (eV) | 1.494 |
| $E_{\mathrm{VB}}$ (eV) | 3.371 |
| $\Delta_{\mathrm{cf}} = \Delta_1$ (w/o SO, meV) | 177 |
| $\Delta_{\mathrm{cf}} = \Delta_1$ (with SO, meV) | 184 |
| $\Delta_2 = \Delta_3$ (meV) | 123 |

the ideal value, $u_{\mathrm{id}} = 0.375$, unlike for most other WZ materials. This is an indication of inverse polarity (and piezoelectricity) in GaAs, consistent with zincblende (ZB) results, for which the piezoelectric coefficient is of opposite sign when compared to the III nitrides. [8]

The band structure of WZ GaAs along high-symmetry lines, with SO coupling, is shown in Fig. 2 (left). A detail of the six topmost valence bands and ten lowest conduction bands around the $\Gamma$ point is given in Fig. 2 (right). Basic band structure information is presented in Table 2. The WZ $\Delta_{1,2,3}$ parameters have been obtained by fitting Eq. (11) of Chuang and Chang [10] to the energy differences obtained from the DFT calculation. The calculation of deformation potentials was carried out without SO coupling. We present results at the $\Gamma$ point only. All the values are given with respect to the average electrostatic (Hartree) potential of the unit cells. The summary of these calculations is presented in Table 2.

## 3   Sixteen-band Hamiltonian for Wurtzite crystals

In order to provide an accurate description of the two energetically close conduction bands closest to the band gap in WZ GaAs within the perturbative approach of the $\mathbf{k} \cdot \mathbf{p}$ formalism beyond the eight-band model, remote conduction bands gain importance due to their coupling to the $\Gamma_8$ conduction band. We have thus employed a sixteen-band model taking the top three $p$-like valence bands, the $\Gamma_7$ and $\Gamma_8$ conduction bands, and the following three $p$-like conduction bands into account, each with their respective $\mid \uparrow \rangle$ and $\mid \downarrow \rangle$ component to a total of sixteen bands. The details of the Hamiltonian can be found together with a schematic plot of bands and coupling terms in Appendix B. In total, 24 parameters need to be determined by fitting to the *ab initio* band structure, namely: $m_{\parallel}^{\mathrm{c}}, m_{\perp}^{\mathrm{c}}, m_{\parallel}, m_{\perp}$ (4), the Luttinger-like parameters $A_i$ and $A_i^{\mathrm{c}}$ with $i = 1..6$ (12), and the optical matrix elements $P_1$,
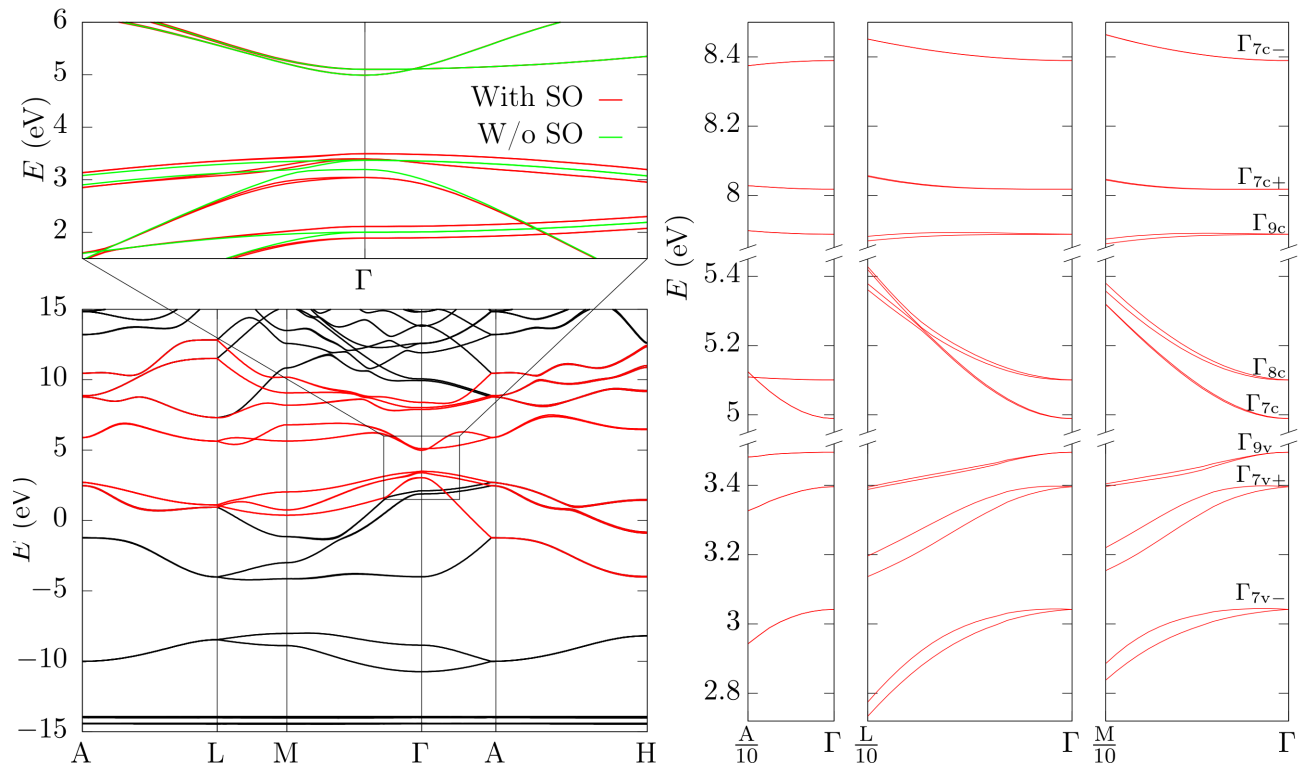
Figure 1: Left: Band structure for WZ GaAs. Relevant bands for the 16-band Hamiltonian are depicted in red. The vicinity of $\Gamma$ is shown in an enlarged view, comparing simulation with (red) and without (green) spin-orbit splitting. Right: Band structure detail around $\Gamma$.

$P_2$, $P_1^c$, $P_2^c$, $P_1'$, $P_2'$, $P_1'''$ and $P_2'''$ (8).

## 4 Multiband parameter extraction

The parameter sets required in $\mathbf{k} \cdot \mathbf{p}$ models of arbitrary complexity can be obtained by fitting the respective $\mathbf{k} \cdot \mathbf{p}$ band structure to an *ab initio* band structure as, e.g., the one obtained in Sec. II. While some of these parameters can be read directly from the band structure at $\Gamma$ (e.g., the band gap, crystal-field and spin-orbit splitting parameters), effective masses and Luttinger-like parameters as well as optical matrix elements can be determined directly from nonlocal empirical pseudopotentials or *ab initio* models with some limitations, [28, 13, 40] but are best determined by numerical fitting. This can be done using gradient minimization schemes readily available in standard mathematics libraries for $\mathbf{k} \cdot \mathbf{p}$ models with a limited level of sophistication as, e.g., six- or eight-band models. However, such schemes commonly fail for more complex multiband-models due to a large number of local minima in the difference between original and fitted band structure spanned by the amount of parameters to be fitted. To avoid trapping in local minima, it is thus necessary to sample the whole, multi-dimensional search space. For the example of an eight-band model for ZB crystals, band gap and spin-orbit splitting can be obtained directly from the band structure, whereas the electron effective mass, $m_\mathrm{e}$, three Luttinger parameters, $\gamma_{1,2,3}$, and the Kane parameter $E_\mathrm{P}$ need to be determined by fitting. With $n_\mathbf{k}$ data points of the *ab initio* input band structure and assuming a discretization of $N$ points in each dimension of the parameter set $P$, we minimize the absolute difference between input

Table 3: Deformation potentials (in the absence of spin-orbit coupling) for WZ GaAs given as the partial derivative of the bands energies at the $\Gamma$ point. All the energies are given with respect to the average Hartree potential of the unit cell. Units are eV.

| Band ordering ($\epsilon = 0$) | Band character | $\frac{\partial(E_i - E_H^{av})}{\partial\epsilon_1}$ | $\frac{\partial(E_i - E_H^{av})}{\partial\epsilon_3}$ | $\frac{\partial(E_i - E_H^{av})}{\partial\epsilon_4}$ | $\frac{\partial(E_i - E_H^{av})}{\partial\epsilon_6}$ |
|---|---|---|---|---|---|
| VBE $-1$ | $z$-like | $-6.39$ | $-13.88$ | $0$ | $0$ |
| VBE | $y$-like | $-6.79$ | $-7.24$ | $0.15$ | $-3.47$ ($[xy]$-like) |
| VBE | $x$-like | $-13.82$ | $-7.24$ | $-0.15$ | $3.47$ ($[x-y]$-like) |
| CBE | $s$-like | $-16.91$ | $-20.30$ | $0$ | $0$ |
| CBE $+1$ | $s$-like | $-17.98$ | $-0.62$ | $0$ | $0$ |
| CBE $+2$ | $x$-like | $-15.11$ | $-4.65$ | $0.20$ | $-3.47$ ($[xy]$-like) |
| CBE $+2$ | $y$-like | $-8.22$ | $-4.65$ | $-0.20$ | $3.47$ ($[x-y]$-like) |
| CBE $+4$ | $z$-like | $-6.32$ | $-17.41$ | $0$ | $0$ |

band structure $\epsilon$ and the one obtained from the fit:

$$v = \sum_{n_{\mathbf{k}}} \text{eig} \left[ \hat{H}_{\mathbf{kp}}(P_i) - \epsilon \right]_{i=1..N} \longrightarrow \text{MIN!} \tag{1}$$

Let us assume that we have a band structure of $n_{\mathbf{k}} = 150$ sample points and that a single eigenvalue problem can be solved within 50 $\mu$s of single-processor time. For an eight-band model for zinc-blende crystals and taking $N = 10$ discretization points in each direction of the five-dimensional parameter set $P$, this results in a computational effort of about 12 min. The computational effort increases exponentially in the numbers of parameters to be fitted. For example, for the WZ structure the dimension of the parameter space doubles and the computational effort would already exceed two years of single processor time. Of course, this minimization problem is perfectly suited for parallelization, but the computational effort nevertheless remains extreme and more sophisticated models than the eight-band formalism, such as full-zone models for indirect band gap semiconductors that require even larger parameter sets, are completely beyond the reach of today's computational capabilities.

This curse of dimensionality can be overcome by stochastic optimization based on randomly chosen search points for the global minimum. Low-discrepancy points are a natural substitute for random numbers. Such quasi-Monte Carlo methods provide a higher accuracy with fewer evaluations of the objective function in Eq. (1). [19] Many practical studies have shown that Sobol points [32, 24] are superior to many other choices of low-discrepancy point sets. For this reason, we search the whole $N_{\text{P}}$-dimensional parameter set $P$ by using properly scaled points from an $N_{\text{P}}$-dimensional Sobol sequence. In this manner, we can keep the number of search points fixed along different dimensionalities of the parameter space, still being able to obtain values close to the global minimum. The respective fitting scheme is illustrated in Fig. 4 for a two-dimensional parameter space. In a first step, the parameter space sampled by the Sobol sequence is spanned by an initial estimate of each parameter together with a respective search range. Some parameters may be known with reasonable accuracy from literature or experience and will have a small surrounding search range whereas this range will be larger for those parameters of which no reference is known. The $N_{\text{P}}$-dimensional Sobol sequence is then mapped on the search ranges of all parameters and the best fit is obtained within all parameter sets defined in this manner (green squares in Fig. 4). Without reducing the size of the search space around all parameters, a new sequence of parameter sets is then spanned around the best suited set obtained before, such that the whole search space moves towards the best set (green squares and blue triangles). Once the best suited parameter set is found and remains unchanged when setting up
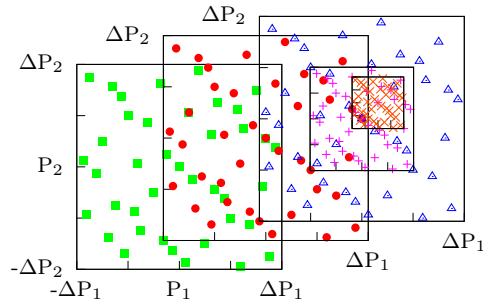
Figure 2: Schematic of the low-discrepancy parameter fitting algorithm. First, the search space is moved with identical ranges until the minimum remains in its center (green squares, red bullets, blue triangles). Once this is achieved, the search space is reduced to increase the accuracy of the parameters (magenta "+" and orange "×").

a new sequence of parameter sets, the search space is reduced by a factor two in each parameter search range such that the numerical accuracy of all parameters increases either to a defined number of search space reductions or until any other chosen convergence criterion is fulfilled (magenta plus and orange crosses).

The objective function in Eq. (1) can furthermore be modified such that priorities of selected $\mathbf{k}$ points as well as those of particular bands that are of pronounced importance, can be increased via individual weights. In order to ensure a good fit at specific high-symmetry points, one can thus easily increase the importance of these points by assigning higher weights to $\mathbf{k}$ values in their vicinity.

Finally, we can evaluate parameter sets within the search space with respect to the degree of non-ellipticity of a Hamiltonian operator employing them.

We demonstrate our fitting scheme for the example of a sixteen-band $\mathbf{k} \cdot \mathbf{p}$ model that takes the top three valence and bottom five conduction bands into account, each with their respective spin-up and spin-down components. We have extracted these bands from the *ab initio* band structure computed above in order to determine the $\mathbf{k} \cdot \mathbf{p}$ parameters for the model as outlined in Appendix B. This particular model requires 24 parameters that are to be fitted to the *ab initio* band structure. The $\mathbf{k} \cdot \mathbf{p}$ Hamiltonian is constructed in a basis consisting of P- and S-like bands. Correspondingly, we first evaluate the orbital character of the *ab initio* bands involved.

Figure 4 shows the character of the *ab initio* bands to which the $\mathbf{k} \cdot \mathbf{p}$ band structure will be fitted. The valence bands $\Gamma_{7v+}$, $\Gamma_{7v-}$, and $\Gamma_{9v}$ exhibit predominantely a P-like character (red solid, dashed, and dash-dotted lines), $\Gamma_{7v+}$ furthermore contains visible S-like contributions (black solid lines). The two conduction bands closest to the band gap, $\Gamma_{7c}$ and $\Gamma_{8c}$, are mostly of S-character, but also with visible P-like contributions. The following conduction band states are predominantly of P-character with S-like contributions in $\Gamma_{9c}$ and $\Gamma_{7c+}$ around the high-symmetry A point. Moreover, nonzero D-like character is seen in these conduction bands (green solid lines), however the impact of D-like bands remains negligible. The character analysis thus reveals that S- and P-like bands in fact represent a reasonable basis for the sixteen band model.

Correspondingly, Fig. 4 shows the sixteen-band $\mathbf{k} \cdot \mathbf{p}$ band structure for WZ GaAs crystals that was fitted to the above *ab initio* band structure. Priority was given to the bands closest to the band gap, namely the bottom two conduction bands and the top two valence bands as they dominate the electronic structure of WZ GaAs. The $\mathbf{k} \cdot \mathbf{p}$ band structure is in good agreement with the *ab initio* one
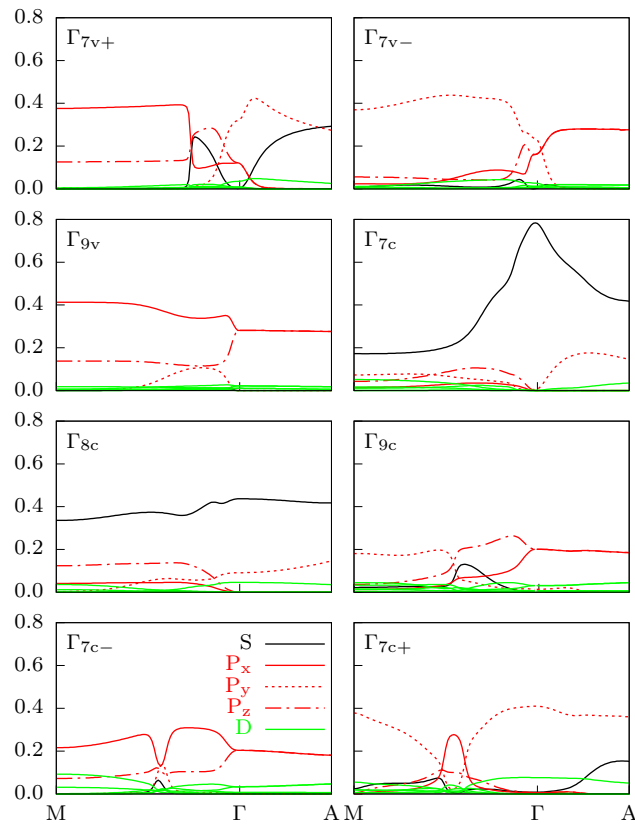
Figure 3: Character of S- (black), P- (red), and D-orbitals (green) of the top six valence and bottom ten conduction bands of the *ab initio* band structure that is used for the fitting procedure. As all bands are pairwise almost degenerate, we evaluate here only one of each pair of bands for the sake of readability. Note that the sum of all contributions to a band is not necessarily one as the underlying atom-centered spherical harmonics do not represent a complete basis.

throughout wide parts of the BZ for the bands of pronounced priority. This is particularly remarkable as the $\mathbf{k} \cdot \mathbf{p}$ perturbation theory commonly allows an accurate description of a band structure only in the close vicinity of high-symmetry points and is not expected to keep this accuracy throughout the BZ. In comparison, the band structure obtained from the initial parameters is depicted in Fig. 4 in blue dashed lines and exhibits very poor agreement with the *ab initio* band structure. It is therefore not necessary to start the minimization with initial parameters that are already close to the final ones, however, the smaller the search range for each parameter, the faster the minimization will deliver a good fit.

The band structure parameters obtained from the fit are presented in Tab. 4 and could, in principle, serve as input for electronic-structure simulations of WZ GaAs heterostructures using the more sophisticated sixteen-band $\mathbf{k} \cdot \mathbf{p}$ model. Details of the initial parameters, search spaces, and priorities can be found in Appendix C.

However, from the curvature of the bands around the BZ boundaries, it can already be expected that spurious solutions will arise if these parameters are employed in a single-particle calculation of a heterostructure. For example, the conduction band bending downwards at the L point will continue deep into the band gap, resulting in energy minima that are a consequence of the incorrect band structure.
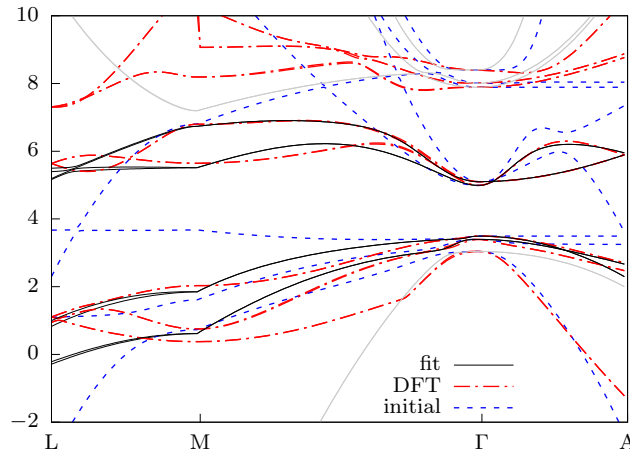
Figure 4: Fit (black and grey solid) of a sixteen-band WZ GaAs $\mathbf{k} \cdot \mathbf{p}$ band structure to the above *ab initio* band structure (red dash-dotted). The blue dashed band structure was obtained from the initial guess parameter set around which the initial Sobol-sequence generated parameter sets were constructed. Priority was given to the four valence and conduction bands closest to the band gap (black solid).

This can also be seen in Fig. 4 where the density of states (DOS) reproduced from the sixteen-band $\mathbf{k} \cdot \mathbf{p}$ band structure above is shown, obtained from sampling throughout the whole BZ. The band gap is indicated with two black solid lines. It can be seen that non-negligible band contributions exist inside the band gap, which is an indicator for the above unphysical band bending somewhere inside the BZ that can potentially induce spurious solutions when a 16-band model with the corresponding material parameters obtained from our fit is applied to study the electronic properties of a nanostructure.

## 5 Ellipticity considerations

In the following, we include ellipticity conditions in our fitting scheme in order to reduce the unphysical DOS inside the band gap. The parameters $\varrho_c$ and $\varrho_v$ as defined in Eq. (21) in Appendix D quantify the degree of non-ellipticity and are thus a measure for the quality of the parameter set with respect to robustness against spurious solutions (for more details see Appendix D), where small values of $\varrho_c$ and $\varrho_v$ represent robust parameter sets. The sum of both, $\varrho = \varrho_c + \varrho_v$ is then multiplied with the cost function $v$ from the initial guess and the parameter $\varepsilon$ that defines the priority to be given to ellipticity. The respective value is then added to the cost function $v$ for each evaluated parameter set. Figure 5 shows the impact of imposing ellipticity conditions on our band structure fit for priority values of $\varepsilon =$0.1, 0.2, and 0.3. It can be seen that an increased priority $\varepsilon$ of the ellipticity conditions in fact reduces the DOS inside the band gap, however, at the cost of a reduced quality of the band structure fit, in particular in the remote areas of the BZ.

If we compare the parameters resulting from the fit (cf. Tab. 4) with literature values where available, [9, 4, 3] we see some significant deviations from existing parameters. In particular, our electron effective masses are quite different from established values, a fact that can also be seen when looking at the band structure in the vicinity of $\Gamma$. However, this is not surprising at this point as the intention of our fitting, and thus the selection of priorities for specific bands and high-symmetry points was to achieve a good fit throughout the whole BZ rather than a good fit of the effective masses at the zone center $\Gamma$.

Table 4: Fitting parameters and band splittings obtained for WZ GaAs within the 16-band $\mathbf{k} \cdot \mathbf{p}$ model. Note that the Kane-like parameters $P_{(1,2)}^{(c,',''')}$ are given in units of eV·Å, whereas the unit in the corresponding script is $E_h \cdot a_0$. The band splitting parameters $\Delta_{1,2,3}^{(c)}$ can be extracted directly from the eigenenergies at $\Gamma$. The splittings $\Delta_{1,2,3}^{cv}$ were found to be negligibly small and are therefore not listed.

| parameter | value | parameter | value |
|---|---|---|---|
| $m_\parallel^e$ ($m_0$) | 0.032 | $m_\parallel^c$ ($m_0$) | 1.117 |
| $m_\perp^e$ ($m_0$) | 0.090 | $m_\perp^c$ ($m_0$) | -0.352 |
| $A_1$ ($\hbar^2/m_0$) | -1.386 | $A_1^c$ ($\hbar^2/m_0$) | -0.951 |
| $A_2$ ($\hbar^2/m_0$) | -0.816 | $A_2^c$ ($\hbar^2/m_0$) | -0.375 |
| $A_3$ ($\hbar^2/m_0$) | 0.003 | $A_3^c$ ($\hbar^2/m_0$) | 4.772 |
| $A_4$ ($\hbar^2/m_0$) | 0.159 | $A_4^c$ ($\hbar^2/m_0$) | 2.687 |
| $A_5$ ($\hbar^2/m_0$) | -1.241 | $A_5^c$ ($\hbar^2/m_0$) | -4.896 |
| $A_6$ ($\hbar^2/m_0$) | 0.176 | $A_6^c$ ($\hbar^2/m_0$) | -0.549 |
| $P_2$ (eV·Å) | 2.405 | $P_2^c$ (eV·Å) | 1.339 |
| $P_1$ (eV·Å) | 1.368 | $P_1^c$ (eV·Å) | 0.058 |
| $P_2'$ (eV·Å) | 0.354 | $P_2'''$ (eV·Å) | 0.796 |
| $P_1'$ (eV·Å) | 0.151 | $P_1'''$ (eV·Å) | 0.642 |
| $\Delta_1$ (eV) | 0.180 | $\Delta_1^c$ (eV) | -0.409 |
| $\Delta_{2,3}$ (eV) | 0.124 | $\Delta_{2,3}^c$ (eV) | -0.074 |

# 6   Parameters for a ten-band model

As the application of a sixteen-band model for the calculation of the electronic properties of a heterostructure represents a much larger computational effort than the well-established eight-band model, we have furthermore extracted a parameter set for a ten-band model required for WZ GaAs and given in detail in Ref. [22] including the top three valence and the bottom two conduction bands in the closer vicinity of the center of the BZ, $\Gamma$. For this model, a total of 13 unknown parameters was determined. The corresponding parameter set is shown in Tab. 5. Of course, the description of the band structure is accurate only in the center of the BZ (cf. Fig. 5) due to the limited basis of the ten-band model. Here, we have also incorporated the ellipticity conditions outlined in Ref. [33] to the valence band part of the Hamiltonian (cf. Eq. (18) in Appendix D) to reduce the risk of spurious solutions if our parameter set is applied to a heterostructure. Ellipticity was here given a priority of $\varepsilon = 0.5$.

We note that our scheme still requires some knowledge on realistic search ranges for each parameter and a fitted parameter set will only be as good as the initial search range chosen for it. In particular, for large search spaces with small initial Sobol sequences, the algorithm can get trapped into local minima and will not see other, global ones. It is thus necessary to carefully evaluate the convergence of the band structure with the number of parameter sets generated using the Sobol sequence. Some of the parameters, e.g., effective masses, can be estimated from the curvature at the $\Gamma$ point, but for others a respectively large search space is required. Moreover, band- and $\mathbf{k}$-point priorities can be adjusted to achieve a good fit only for some of the bands employed, leaving both a certain degree of arbitrariness in the fitting process and large deviations from the *ab initio* band structure for bands of low priority (cf. grey bands in Fig. 4).
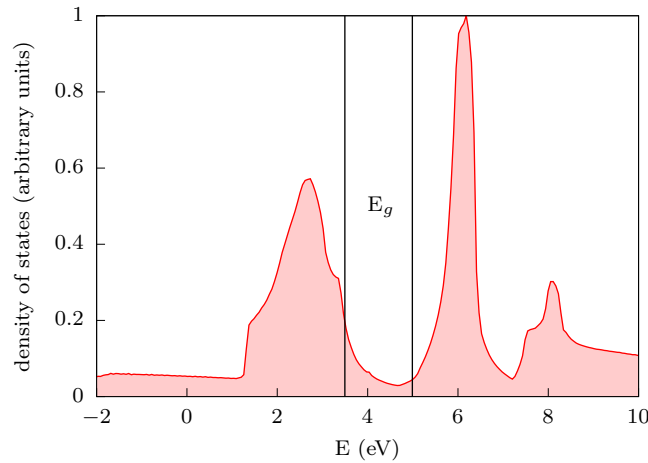
Figure 5: Density of states of the $\mathbf{k} \cdot \mathbf{p}$ band structure of the sixteen-band model shown in Fig. 4.
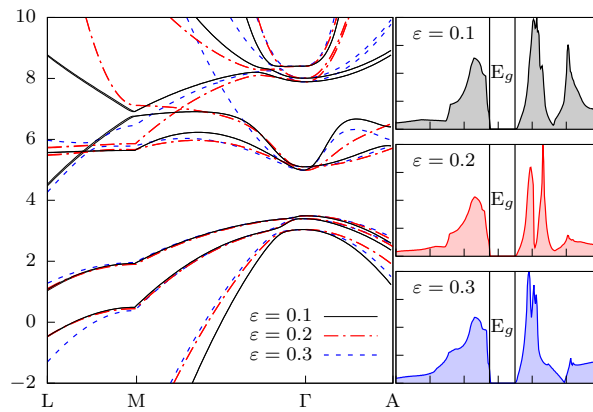


Figure 6: Left: band structures obtained from fitting for $\varepsilon = 0.1$ (black solid), 0.2 (red dash-dotted), and 0.3 (blue dashed line). Right: the respective density of states.

# 7 Summary

We have presented a numerically efficient fitting scheme to obtain $\mathbf{k} \cdot \mathbf{p}$ electronic structure parameters for multi-band $\mathbf{k} \cdot \mathbf{p}$ models beyond the well-established eight-band approach from up-to-date *ab initio* band structures. Our scheme employs low-discrepancy sequences to sample multi-dimensional parameter spaces for more sophisticated $\mathbf{k} \cdot \mathbf{p}$ models. In addition, it allows direct control of priorities of specific $\mathbf{k}$-points and bands that are of pronounced importance for the electronic structure to ensure a highly accurate fit within selected regions. Furthermore, the likelihood to encounter spurious solutions can be reduced by introducing non-ellipticity conditions during the fitting process. We have presented material parameters for both a 16-band $\mathbf{k} \cdot \mathbf{p}$ model that was developed within this work as well as a ten-band model which is better suited for computationally inexpensive simulations of the electronic structure of heterostructures containing GaAs in the WZ phase. Finally, we remark that our scheme is not limited to semiconductors but can provide parameters for all band structures that can be computed from a Hamiltonian.

Table 5: Fitting parameters obtained for WZ GaAs within the ten-band $\mathbf{k} \cdot \mathbf{p}$ model. The parameter $P_2^{cv}$ couples the $\Gamma_8$ conduction band to the top $\Gamma_{9v}$ valence band within the ten-band model employed (the Hamiltonian is given in Ref. [22], $P_2^{cv}$ here enters via: $R = i(\partial_x + i\partial y)P_2^{cv}$).

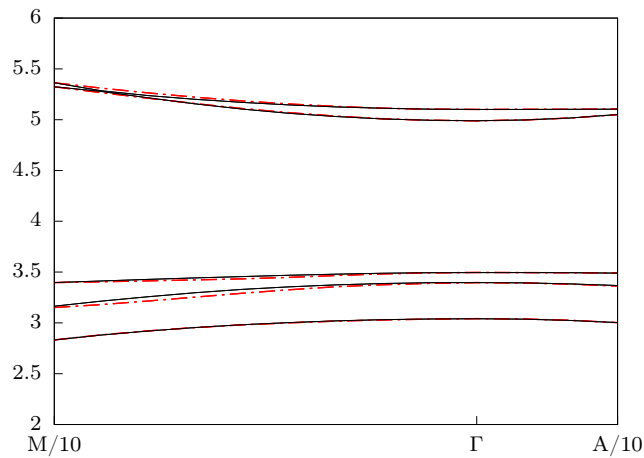| parameter | value | parameter | value |
|---|---|---|---|
| $m_\parallel^e$ ($m_0$) | 0.0582 | $A_1$ ($\hbar^2/m_0$) | -13.666 |
| $m_\perp^e$ ($m_0$) | 0.0979 | $A_2$ ($\hbar^2/m_0$) | -7.088 |
| $m_\parallel^c$ ($m_0$) | 2.549 | $A_3$ ($\hbar^2/m_0$) | 6.972 |
| $m_\perp^c$ ($m_0$) | 0.1276 | $A_4$ ($\hbar^2/m_0$) | 2.727 |
| $P_1$ (eV·Å) | 2.270 | $A_5$ ($\hbar^2/m_0$) | 4.952 |
| $P_2$ (eV·Å) | 2.996 | $A_6$ ($\hbar^2/m_0$) | 2.641 |
| $P_2^{cv}$ (eV·Å) | 1.301 | | |



Figure 7: *Ab initio* band structure (red dash-dotted) and fit using a ten-band $\mathbf{k} \cdot \mathbf{p}$ model (black solid) in the vicinity of $\Gamma$. The respective parameters are listed in Tab. 5.

# Appendix

## 7.1 Density functional theory

In view of the scarcity of data available on WZ GaAs, to accurately model its electronic structure we fitted the screening parameter $\mu$ of the HSE hybrid functional [15] to yield the experimental zero-temperature band gap for ZB GaAs first, which is well established at 1.519 eV. This is achieved in our calculations, in the absence of spin-orbit (SO) coupling, for $\mu = 0.138$ Å$^{-1}$. However, SO coupling reduces the size of the band gap, which means a lower value of $\mu$ is required to reproduce the experimental gap with the SO interaction enabled. Therefore we chose $\mu = 0.089$ Å$^{-1}$, which yields a good agreement with the experimental value. Compared to the $\mu = 0.3$ Å$^{-1}$ and $\mu = 0.2$ Å$^{-1}$ screening parameters of HSE03 and HSE06, our customized functional is less screened. We explored a combined optimization of screening parameter and mixing parameter $\alpha$, to try and improve the simultaneous description of both band gap and lattice parameter. However, only marginal improvement was achieved for reasonable values of $\alpha$. Perfect agreement for both quantities without SO coupling was obtained for the tuple $(\mu, \alpha) = (0.8$ Å$^{-1}, 1.45)$. In view of the difficulty to optimize both parameters and the fact that the choice of $\alpha = 0.25$ is theoretically justified, [26] we decided to settle

for $(\mu, \alpha) = (0.089 \text{ Å}^{-1}, 0.25)$. The DFT code used was VASP, [17] which is based on projector-augmented wave (PAW) potentials [5, 18] and plane-wave basis sets. We chose a cutoff energy for the plane waves of 350 eV. The grids used for Brillouin zone (BZ) integration were chosen differently for structural and elastic properties (finer mesh) and electronic structure (coarser mesh). For a GaAs ZB primitive unit cell (two atoms) we found that a $10 \times 10 \times 10$ mesh was enough to converge the total energy below 0.1 meV. For the electronic structure calculations, we used a $6 \times 6 \times 6$ mesh. The motivation for using a finer $k$-mesh for structural properties is twofold. First, band structures are less sensitive to the density of $k$ points used. Second, for spin-orbit calculations, the spin-orbit coupling breaks the symmetry of the BZ, leading to a significantly larger number of non-equivalent $k$ points; using dense grids becomes prohibitively expensive. For the evaluation of the Coulomb kernel (for the exact-exchange calculation) we used a $k$-point reduction scheme whereby the number of $k$ points in the grid was halved along each reciprocal lattice direction. This is known as "downsampling". [25] All the other simulations were carried out maintaining a density of $k$ points as close as possible to those specified above. The semicore $d$ electrons of Ga were included explicitly in the calculation as valence electrons.

## 7.2 Sixteen-band Hamiltonian

We start with the assumption that the relevant near-band gap states are spanned by the $p$-like valence bands $X_\text{v}$, $Y_\text{v}$, $Z_\text{v}$ followed by the $s$-like conduction band $S$ (commonly the conduction band closest to the band gap), three $p$-like conduction bands $X_\text{c}$, $Y_\text{c}$ and $Z_\text{c}$ and another $s$-like band $S'$. We follow the procedure used in Ref. [10] with the basis set:
$|S \uparrow\rangle, |X_\text{v} \uparrow\rangle, |Y_\text{v} \uparrow\rangle, |Z_\text{v} \uparrow\rangle, |S \downarrow\rangle, |X_\text{v} \downarrow\rangle, |Y_\text{v} \downarrow\rangle, |Z_\text{v} \downarrow\rangle$ for the top $p$-like valence bands and the (commonly bottom) $s$-like conduction band and $|S' \uparrow\rangle, |X_\text{c} \uparrow\rangle, |Y_\text{c} \uparrow\rangle, |Z_\text{c} \uparrow\rangle, |S' \downarrow\rangle, |X_\text{c} \downarrow\rangle, |Y_\text{c} \downarrow\rangle, |Z_\text{c} \downarrow\rangle$ for the respective following conduction bands. The Hamiltonian then reads:

$$\hat{H} = \begin{pmatrix} G_1^\text{c}(\mathbf{k}) + G_2^\text{c}(\mathbf{k}) & \Gamma \\ -\Gamma^\dagger & G_1(\mathbf{k}) + G_2(\mathbf{k}) \end{pmatrix} \tag{2}$$

with:

$$G_1^\text{c}(\mathbf{k}) = \begin{pmatrix} E_1^\text{c} & iP_2^\text{c}k_x & iP_2^\text{c}k_y & iP_1^\text{c}k_z & 0 & 0 & 0 & 0 \\ -iP_2^\text{c}k_x & E_2^\text{c} & -i\Delta_2^\text{c} & 0 & 0 & 0 & 0 & \Delta_3^\text{c} \\ -iP_2^\text{c}k_y & i\Delta_2^\text{c} & E_2^\text{c} & 0 & 0 & 0 & 0 & -i\Delta_3^\text{c} \\ -iP_1^\text{c}k_z & 0 & 0 & E_2^\text{c} - \Delta_\text{CF}^\text{c} & 0 & -\Delta_3^\text{c} & i\Delta_3^\text{c} & 0 \\ 0 & 0 & 0 & 0 & E_1^\text{c} & iP_2^\text{c}k_x & iP_2^\text{c}k_y & iP_1^\text{c}k_z \\ 0 & 0 & 0 & -\Delta_3^\text{c} & -iP_2^\text{c}k_x & E_2^\text{c} & i\Delta_2^\text{c} & 0 \\ 0 & 0 & 0 & -i\Delta_3^\text{c} & -iP_2^\text{c}k_y & -i\Delta_2^\text{c} & E_2^\text{c} & 0 \\ 0 & \Delta_3^\text{c} & i\Delta_3^\text{c} & 0 & -iP_1^\text{c}k_z & 0 & 0 & E_2^\text{c} - \Delta_\text{CF}^\text{c} \end{pmatrix}$$

$$G_2^\text{c}(\mathbf{k}) = \begin{pmatrix} G''^\text{c}_2(\mathbf{k}) & 0 \\ 0 & G''^{\text{c}\dagger}_2(\mathbf{k}) \end{pmatrix} \text{ with:}$$

$$G''^\text{c}_2(\mathbf{k}) = \begin{pmatrix} \tilde{A}_2^\text{c}(k_x^2 + k_y^2) + \tilde{A}_1^\text{c}k_z^2 & B_x^\text{c}k_yk_z & B_x^\text{c}k_xk_z & B_z^\text{c}k_xk_y \\ B_x^\text{c}k_yk_z & L_1^\text{c}k_x^2 + M_1^\text{c}k_y^2 + M_2^\text{c}k_z^2 & N_1^\text{c}k_xk_y & N_2^\text{c}k_xk_z - N_3^\text{c}k_x \\ B_x^\text{c}k_xk_z & N_1^\text{c}k_xk_y & M_1^\text{c}k_x^2 + L_1^\text{c}k_y^2 + M_2^\text{c}k_z^2 & N_2^\text{c}k_yk_z + N_3^\text{c}k_y \\ B_z^\text{c}k_xk_y & N_2^\text{c}k_xk_z + N_3^\text{c}k_x & N_2^\text{c}k_yk_z - N_3^\text{c}k_y & M_3^\text{c}(k_x^2 + k_y^2) + L_2^\text{c}k_z^2 \end{pmatrix}$$

The elements $\tilde{A}^{\mathrm{c}}_{(1,2)}$, $L^{\mathrm{c}}_{(1,2)}$, $M^{\mathrm{c}}_{(1,2,3)}$, and $N^{\mathrm{c}}_{(1,2,3)}$ are given by:

$$\tilde{A}^{\mathrm{c}}_1 = \frac{1}{2m^{\mathrm{c}}_\parallel} - \frac{(P^{\mathrm{c}}_2)^2}{E_2 - E_1} \quad \text{and} \quad \tilde{A}^{\mathrm{c}}_2 = \frac{1}{2m^{\mathrm{c}}_\perp} - \frac{(P^{\mathrm{c}}_1)^2}{E_2 - E_1} \tag{3}$$

$$L^{\mathrm{c}}_1 = \frac{1}{2}\left(A^{\mathrm{c}}_2 + A^{\mathrm{c}}_4 + A^{\mathrm{c}}_5\right) - \frac{(P^{\mathrm{c}}_1)^2}{E_2 - E_1} \quad \text{and} \quad L^{\mathrm{c}}_2 = \frac{1}{2}A^{\mathrm{c}}_1 + \frac{(P^{\mathrm{c}}_2)^2}{E_2 - E_1} \tag{4}$$

$$M^{\mathrm{c}}_1 = \frac{1}{2}\left(A^{\mathrm{c}}_2 + A^{\mathrm{c}}_4 - A^{\mathrm{c}}_5\right), \quad M^{\mathrm{c}}_2 = \frac{1}{2}\left(A^{\mathrm{c}}_1 + A^{\mathrm{c}}_3\right), \text{ and } \quad M^{\mathrm{c}}_3 = \frac{1}{2}A^{\mathrm{c}}_2 \tag{5}$$

$$N^{\mathrm{c}}_1 = \frac{1}{2}A^{\mathrm{c}}_5 + \frac{(P^{\mathrm{c}}_2)^2}{E_2 - E_1}, \quad N^{\mathrm{c}}_2 = \frac{1}{\sqrt{2}}A^{\mathrm{c}}_6 + \frac{P^{\mathrm{c}}_1 P^{\mathrm{c}}_2}{E_2 - E_1} \quad \text{and} \quad N^{\mathrm{c}}_3 = i\sqrt{2}A^{\mathrm{c}}_7 \tag{6}$$

And similarly:

$$G_1(\mathbf{k}) = \begin{pmatrix} E_{\mathrm{g}} & iP_2 k_x & iP_2 k_y & iP_1 k_z & 0 & 0 & 0 & 0 \\ -iP_2 k_x & 0 & -i\Delta_2 & 0 & 0 & 0 & 0 & \Delta_3 \\ -iP_2 k_y & i\Delta_2 & 0 & 0 & 0 & 0 & 0 & -i\Delta_3 \\ -iP_1 k_z & 0 & 0 & -\Delta_{\mathrm{CF}} & 0 & -\Delta_3 & i\Delta_3 & 0 \\ 0 & 0 & 0 & 0 & E_{\mathrm{g}} & iP_2 k_x & iP_2 k_y & iP_1 k_z \\ 0 & 0 & 0 & -\Delta_3 & -iP_2 k_x & 0 & i\Delta_2 & 0 \\ 0 & 0 & 0 & -i\Delta_3 & -iP_2 k_y & -i\Delta_2 & 0 & 0 \\ 0 & \Delta_3 & i\Delta_3 & 0 & -iP_1 k_z & 0 & 0 & -\Delta_{\mathrm{CF}} \end{pmatrix}$$

$$G_2(\mathbf{k}) = \begin{pmatrix} G'_2(\mathbf{k}) & 0 \\ 0 & G'^{\dagger}_2(\mathbf{k}) \end{pmatrix} \quad \text{with:}$$

$$G'_2(\mathbf{k}) = \begin{pmatrix} \tilde{A}_2(k_x^2 + k_y^2) + \tilde{A}_1 k_z^2 & B_{\mathsf{x}} k_y k_z & B_{\mathsf{x}} k_x k_z & B_{\mathsf{z}} k_x k_y \\ B_{\mathsf{x}} k_y k_z & L_1 k_x^2 + M_1 k_y^2 + M_2 k_z^2 & N_1 k_x k_y & N_2 k_x k_z - N_3 k_x \\ B_{\mathsf{x}} k_x k_z & N_1 k_x k_y & M_1 k_x^2 + L_1 k_y^2 + M_2 k_z^2 & N_2 k_y k_z + N_3 k_y \\ B_{\mathsf{z}} k_x k_y & N_2 k_x k_z + N_3 k_x & N_2 k_y k_z - N_3 k_y & M_3(k_x^2 + k_y^2) + L_2 k_z^2 \end{pmatrix}$$

Again, $\tilde{A}_{(1,2)}$, $L_{(1,2)}$, $M_{(1,2,3)}$, and $N_{(1,2,3)}$ are given by:

$$\tilde{A}_1 = \frac{1}{2m_\parallel} - \frac{P_2^2}{E_{\mathrm{g}}} \quad \text{and} \quad \tilde{A}_2 = \frac{1}{2m_\perp} - \frac{P_1^2}{E_{\mathrm{g}}} \tag{7}$$

$$L_1 = \frac{1}{2}\left(A_2 + A_4 + A_5\right) - \frac{P_1^2}{E_{\mathrm{g}}} \quad \text{and} \quad L_2 = \frac{1}{2}A_1 + \frac{P_2^2}{E_{\mathrm{g}}} \tag{8}$$

$$M_1 = \frac{1}{2}\left(A_2 + A_4 - A_5\right), \quad M_2 = \frac{1}{2}\left(A_1 + A_3\right), \text{ and } \quad M_3 = \frac{1}{2}A_2 \tag{9}$$

$$N_1 = \frac{1}{2}A_5 + \frac{P_2^2}{E_{\mathrm{g}}}, \quad N_2 = \frac{1}{\sqrt{2}}A_6 + \frac{P_1 P_2}{E_{\mathrm{g}}} \quad \text{and} \quad N_3 = i\sqrt{2}A_7 \tag{10}$$

From symmetry considerations the $B$ terms are zero. The commonly small parameter $A_7$ as well as its counterpart in the upper conduction bands, $A^{\mathrm{c}}_7$, were also set to zero. This follows from for $B_x$: $\langle S|\mathbf{k} \cdot \mathbf{p}|i\rangle\langle i|\mathbf{k} \cdot \mathbf{p}|X\rangle = k_y k_z \langle S|p_y|Y\rangle\langle Y|p_z|X\rangle + k_y k_z \langle S|p_z|Z\rangle\langle Z|p_y|X\rangle$, and that a reflection in the x-z-plane: y→-y, x→x, z→z is a symmetry of WZ such that $\langle Y|p_z|X\rangle = \langle Z|p_y|X\rangle = 0$. The
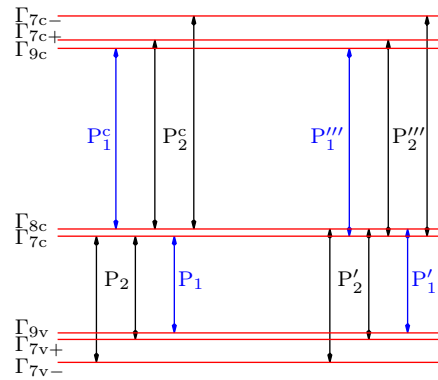
Figure 8: Term scheme of basis bands and coupling elements.

coupling between the upper and the lower eight bands is realized via:

$$\Gamma(\mathbf{k}) = \begin{pmatrix} 0 & iP_2'k_x & iP_2'k_y & iP_1'k_z & 0 & 0 & 0 & 0 \\ -iP_2'''k_x & 0 & -i\Delta_2^{cv} & 0 & 0 & 0 & 0 & \Delta_{3,1}^{cv} \\ -iP_2'''k_y & i\Delta_2^{cv} & 0 & 0 & 0 & 0 & 0 & -i\Delta_{3,1}^{cv} \\ -iP_1'''k_z & 0 & 0 & 0 & 0 & -\Delta_{3,2}^{cv} & i\Delta_{3,2}^{cv} & 0 \\ 0 & 0 & 0 & 0 & 0 & iP_2'''k_x & iP_2'''k_y & iP_1'''k_z \\ 0 & 0 & 0 & \Delta_{3,1}^{cv} & -iP_2'k_x & 0' & i\Delta_2^{cv} & 0 \\ 0 & 0 & 0 & -i\Delta_{3,1}^{cv} & -iP_2'k_y & -i\Delta_2^{cv} & 0 & 0 \\ 0 & \Delta_{3,2}^{cv} & i\Delta_{3,2}^{cv} & 0 & -iP_1'k_z & 0 & 0 & 0 \end{pmatrix}$$

A schematic view of basis functions and respective couplings is shown in Fig. 7.2. Note that the small, but nonzero coupling of the $\Gamma_{8c}$ and the $\Gamma_{9v}$ as well as the corresponding $\Gamma_{7c}$ and $\Gamma_{9c}$ is neglected.

## 7.3   Conditions and initial data for the parameter fitting

The parameter fitting algorithm has a number of parameters that can be adjusted to achieve a particularly good representation of selected parts of the band structure. For the band structure shown in Fig. 4, these were the following: First, the priority of the top four valence bands has been set to 1000, and for the bottom four conduction bands to 2000, while the default applied to the other bands is 1. In the respective output of the fit in Fig. 4, black solid lines indicate those with larger priority whereas the others are depicted in gray. Furthermore, priority was given to the M, $\Gamma$, and A points and another two points between M and $\Gamma$ where a Gaussian function was multiplied to Eq. (1) with a peak value of 1000. The parameter space was mapped onto a Sobol sequence of 10000 elements. With these data, the fitting of all parameters for a band structure with 182 sampling points takes about 60 min on a single CPU.

## 7.4   Ellipticity conditions

A linear differential operator of second order as it occurs structurally, e.g., as a component of a multiband $\mathbf{k} \cdot \mathbf{p}$ Hamiltonian, that acts on a scalar function $u(\mathbf{x})$ defined as: [33, 35]

$$\left( -\sum_{i,j=1}^{n} \partial_i a_{ij}(\mathbf{x})\partial_j + \sum_{i=1}^{n} b_i(\mathbf{x})\partial_i + c(\mathbf{x}) \right) u(\mathbf{x}) \tag{11}$$

Table 6: Initial values, search space ranges, and final fitting parameters obtained for WZ GaAs within the 16-band $\mathbf{k} \cdot \mathbf{p}$ model.

| parameter | initial | range | final, $\varepsilon = 0$ | $\varepsilon = 0.1$ |
|---|---|---|---|---|
| $m_\parallel^e$ ($m_0$) | 0.04 | 0.01 | 0.032 | 0.042 |
| $m_\perp^e$ ($m_0$) | 0.1 | 0.01 | 0.090 | 0.100 |
| $A_1$ ($\hbar^2/m_0$) | -5 | 2 | -1.386 | -2.148 |
| $A_2$ ($\hbar^2/m_0$) | -0.5 | 0.4 | -0.816 | -0.855 |
| $A_3$ ($\hbar^2/m_0$) | 5 | 4 | 0.003 | 1.104 |
| $A_4$ ($\hbar^2/m_0$) | 0.5 | 0.4 | 0.159 | 0.007 |
| $A_5$ ($\hbar^2/m_0$) | -0.5 | 0.4 | -1.241 | -0.855 |
| $A_6$ ($\hbar^2/m_0$) | -0.5 | 0.2 | 0.176 | -0.753 |
| $P_1$ (eV·Å) | 1.44 | 0.288 | 2.405 | 1.379 |
| $P_2$ (eV·Å) | 1.44 | 0.288 | 1.368 | 0.229 |
| $m_\parallel^c$ ($m_0$) | 1.0 | 0.2 | 1.117 | 1.378 |
| $m_\perp^c$ ($m_0$) | 0.1 | 0.3 | -0.352 | -0.561 |
| $A_1^c$ ($\hbar^2/m_0$) | -5 | 2 | -0.951 | -1.361 |
| $A_2^c$ ($\hbar^2/m_0$) | -0.5 | 0.2 | -0.375 | -0.466 |
| $A_3^c$ ($\hbar^2/m_0$) | 5 | 2 | 4.772 | 2.374 |
| $A_4^c$ ($\hbar^2/m_0$) | 5 | 2 | 2.687 | 1.234 |
| $A_5^c$ ($\hbar^2/m_0$) | -5 | 2 | -4.896 | -1.539 |
| $A_6^c$ ($\hbar^2/m_0$) | -0.5 | 0.2 | -0.549 | -0.559 |
| $P_1^c$ (eV·Å) | 1.44 | 3.60 | 1.339 | 0.017 |
| $P_2^c$ (eV·Å) | 1.44 | 3.60 | 0.058 | 0.704 |
| $P_1'$ (eV·Å) | 7.2 | 2.88 | 8.035 | 6.847 |
| $P_1'''$ (eV·Å) | 7.2 | 2.88 | 1.498 | 5.490 |
| $P_2'$ (eV·Å) | 7.2 | 2.88 | 6.134 | 2.570 |
| $P_2'''$ (eV·Å) | 7.2 | 2.88 | 13.939 | 9.421 |

is called elliptic if the second-order differential operator matrix $\mathbf{K}(a_{ij}(\mathbf{k}))$ is positive definite. [33] If one then assumes $u$ to be defined inside a region $\Omega$ and zero at its boundary $\partial\Omega$, left multiplying the second-order terms of Eq. (11) with a test function $v^\star$ and integrating over the region yields

$$\alpha(u,v) := \int_\Omega \sum_{i,j=1}^n \partial_i v^\star a_{ij}(\mathbf{x}) \partial_j u \, d\Omega. \tag{12}$$

For an elliptic operator and a normed function space $V$, this bilinear form is convex:

$$\alpha(u,v) > C||u||_V \ \forall \, u \in \, V. \tag{13}$$

Rewriting Eq. (12) in matrix form using the differential operator matrix $\mathbf{K}$ we obtain:

$$\alpha(u,v) = \int_\Omega (\partial_x v^\star \partial_y v^\star \partial_z v^\star) \mathbf{K} \begin{pmatrix} \partial_x u \\ \partial_y u \\ \partial_z u \end{pmatrix} d\Omega. \tag{14}$$

If $\mathbf{K}$ is positive definite for all $\mathbf{x}$, $\alpha(\dot{;})$ will be convex. Within a heterostructure, the coupled differential equation system is defined within an envelope function vector $\mathbf{f}$. The analogy to Eq. (12) here

reads: [33]

$$\hat{\alpha}(\mathbf{f}, \mathbf{v}) = \int_\Omega \sum_{ijkl} \partial_i v_k^\star h_{ij}^{kl} \partial_j f_l d\Omega \tag{15}$$

with $h_{ij}^{kl} = (\mathbf{H}_{ij}^{(2)})_{kl}$ where $k$ and $l$ are the indices of the $m$ Bloch bands involved and $i$ and $j = x, y, z$. For a system quantized in all three directions, the matrix form of Eq. (15) is given by:

$$\hat{\alpha}(\mathbf{u}, \mathbf{v}) = \int_\Omega (\partial_x v_1^\star \partial_y v_1^\star ... \partial_y v_m^\star \partial_z v_m^\star) \tag{16}$$

$$\times \begin{pmatrix} h_{11}^{11} & h_{12}^{11} & \cdots & h_{12}^{1m} & h_{13}^{1m} \\ h_{21}^{11} & h_{22}^{11} & \cdots & h_{22}^{1m} & h_{23}^{1m} \\ \vdots & \vdots & \ddots & \vdots & \vdots \\ h_{21}^{m1} & h_{22}^{m1} & \cdots & h_{22}^{mm} & h_{23}^{mm} \\ h_{31}^{m1} & h_{32}^{m1} & \cdots & h_{32}^{mm} & h_{33}^{mm} \end{pmatrix} \begin{pmatrix} \partial_x u_1 \\ \partial_y u_1 \\ \vdots \\ \partial_y u_m \\ \partial_z u_m \end{pmatrix} \partial\Omega \tag{17}$$

and has strictly positive eigenvalues if the matrix defined by $h_{ij}^{kl}$ is positive definite. For Hamiltonians related to the valence band, the available energy spectrum ranges from $-\infty$ to the valence band maximum so that for these cases Eq. (17) has to be negative definite. For the eight-band model, however, the range of accessible energies ranges from $-\infty$ to $+\infty$ so that no upper or lower boundaries for the eigenvalues exist. Here, the conduction band and valence band parts of the Hamiltonian need to be decoupled so that energy spectra of both band types can be evaluated separately. [33]

We have modified the scheme from Ref. [33] to our 16-band Hamiltonian as defined in Eq. (2) above. Following the considerations in Ref. [33], all contributions quadratic in $\mathbf{k}$ enter the Hamiltonian in either the two $6 \times 6$ matrices for the p-like valence and conduction band states or in the $2 \times 2$ matrices for the s-like conduction bands. The s-like conduction band related matrices are furthermore not coupled to each other whereas the two $6 \times 6$ matrices are in fact each two $3 \times 3$ matrices that lack second-order coupling. Correspondingly, the eigenvalues of the valence-band related matrix

$$h_{ij,\mathbf{v}}^{kl} = \begin{pmatrix} L_1 & 0 & 0 & 0 & N_1^+ & 0 & 0 & 0 & N_2^+ \\ 0 & M_1 & 0 & N_1^- & 0 & 0 & 0 & 0 & 0 \\ 0 & 0 & M_2 & 0 & 0 & 0 & N_2^- & 0 & 0 \\ 0 & N_1^- & 0 & M_1 & 0 & 0 & 0 & 0 & 0 \\ N_1^+ & 0 & 0 & 0 & L_1 & 0 & 0 & 0 & N_2^+ \\ 0 & 0 & 0 & 0 & 0 & M_2 & 0 & N_2^- & 0 \\ 0 & 0 & N_2^- & 0 & 0 & 0 & M_3 & 0 & 0 \\ 0 & 0 & 0 & 0 & 0 & N_2^- & 0 & M_3 & 0 \\ N_2^+ & 0 & 0 & 0 & N_2^+ & 0 & 0 & 0 & L_2 \end{pmatrix} \tag{18}$$

are preferably required to be negative such that

$$\varrho_{\mathbf{v}} = \left| \frac{\sum_{i, \lambda_i > 0} \lambda_i}{\sum_{j, \lambda_j < 0} \lambda_j} \right|, \tag{19}$$

which is an estimate for the degree of nonconvexity, is as small as possible and ideally zero. For the

five conduction bands in the model, the related matrix reads:

$$h_{ij,\mathrm{v}}^{kl} = \begin{pmatrix}
L_1^c & 0 & 0 & 0 & N_1^{c+} & 0 & 0 & 0 & N_2^{c+} & 0 & 0 & 0 & 0 & 0 & 0 \\
0 & M_1^c & 0 & N_1^{c-} & 0 & 0 & 0 & 0 & 0 & 0 & 0 & 0 & 0 & 0 & 0 \\
0 & 0 & M_2^c & 0 & 0 & 0 & N_2^{c-} & 0 & 0 & 0 & 0 & 0 & 0 & 0 & 0 \\
0 & N_1^{c-} & 0 & M_1^c & 0 & 0 & 0 & 0 & 0 & 0 & 0 & 0 & 0 & 0 & 0 \\
N_1^{c+} & 0 & 0 & 0 & L_1^c & 0 & 0 & 0 & N_2^{c+} & 0 & 0 & 0 & 0 & 0 & 0 \\
0 & 0 & 0 & 0 & 0 & M_2^c & 0 & N_2^{c-} & 0 & 0 & 0 & 0 & 0 & 0 & 0 \\
0 & 0 & N_2^{c-} & 0 & 0 & 0 & M_3^c & 0 & 0 & 0 & 0 & 0 & 0 & 0 & 0 \\
0 & 0 & 0 & 0 & 0 & N_2^{c-} & 0 & M_3^c & 0 & 0 & 0 & 0 & 0 & 0 & 0 \\
N_2^{c+} & 0 & 0 & 0 & N_2^{c+} & 0 & 0 & 0 & L_2^c & 0 & 0 & 0 & 0 & 0 & 0 \\
0 & 0 & 0 & 0 & 0 & 0 & 0 & 0 & 0 & A_1^c & 0 & 0 & 0 & 0 & 0 \\
0 & 0 & 0 & 0 & 0 & 0 & 0 & 0 & 0 & 0 & A_1^c & 0 & 0 & 0 & 0 \\
0 & 0 & 0 & 0 & 0 & 0 & 0 & 0 & 0 & 0 & 0 & A_2^c & 0 & 0 & 0 \\
0 & 0 & 0 & 0 & 0 & 0 & 0 & 0 & 0 & 0 & 0 & 0 & A_1 & 0 & 0 \\
0 & 0 & 0 & 0 & 0 & 0 & 0 & 0 & 0 & 0 & 0 & 0 & 0 & A_1 & 0 \\
0 & 0 & 0 & 0 & 0 & 0 & 0 & 0 & 0 & 0 & 0 & 0 & 0 & 0 & A_2
\end{pmatrix} \tag{20}$$

with its eigenvalues being preferably positive such that

$$\varrho_{\mathrm{c}} = \left| \frac{\sum_{i,\lambda_i<0} \lambda_i}{\sum_{j,\lambda_j>0} \lambda_j} \right|. \tag{21}$$

Finally, we sum up both conditions to $\varrho = \varrho_{\mathrm{v}} + \varrho_{\mathrm{c}}$ as a total estimate of the degree of nonconvexity. Note that $N_{(1,2)}^{(c)\pm} = N_{(1,2)}^{(c)}$, as a detailed discussion of asymmetric operator ordering as discussed in Refs. [33, 34, 35] or a spectral analysis of the Hamiltonian as discussed in Ref. [2] is beyond the scope of the present work. However, our fitting scheme can be modified to identify the best parameters for asymmetric operators as well in a straight-forward manner.

# References

[1] A. D. Andreev and E. P. O'Reilly. *Phys. Rev. B*, 62:15851, 2000.

[2] U. Bandelow, H. C. Kaiser, T. Koprucki, and J. Rehberg. *Numerical Functional Analysis and Optimization*, 21(3-4):379–409, 2000.

[3] F. Bechstedt and A. Belabbes. *Journal of Physics: Condensed Matter*, 25(27):273201, 2013.

[4] A. Belabbes, C. Panse, J. Furthmüller, and F. Bechstedt. *Phys. Rev. B*, 86:075208, Aug 2012.

[5] P. E. Blöchl. *Phys. Rev. B*, 50:17953, 1999.

[6] M. Cardona and F. H. Pollak. *Phys. Rev.*, 142:530–543, Feb 1966.

[7] M. A. Caro, S. Schulz, and E. P. O'Reilly. *J. Phys.: Condens. Matter*, 25:025803, 2013.

[8] M. A. Caro, S. Schulz, and E. P. O'Reilly. *Phys. Rev. B*, 91:075203, 2015.

[9] T. Cheiwchanchamnangij and W. R. L. Lambrecht. *Phys. Rev. B*, 84:035203, Jul 2011.

[10] S. L. Chuang and C. S. Chang. *Phys. Rev. B*, 54:2491, 1996.

[11] P. Corfdir, B. V. Hattem, E. Uccelli, S. Conesa-Boj, P. Lefebvre, A. F. i Morral, and R. T. Phillips. *Nano Lett.*, 13:5303, 2013.

[12] P. Corfdir, O. Marquardt, R. B. Lewis, C. Sinito, M. Ramsteiner, A. Trampert, U. Jahn, L. Geelhaar, O. Brandt, and V. M. Fomin. *Adv. Mater.*, 31:1805645, 2019.

[13] D. J. Dugdale, S. Brand, and R. A. Abram. *Phys. Rev. B*, 61:12933, 2000.

[14] V. A. Fonoberov and A. A. Balandin. *J. Appl. Phys.*, 94:7178, 2003.

[15] J. Heyd, G. E. Scuseria, and M. Ernzerhof. *J. Chem. Phys.*, 118:8207, 2003.

[16] S. Z. Karazhanov and L. C. Lew Yan Voon. *Semiconductors*, 39(2):161–173, Feb 2005.

[17] G. Kresse and J. Furthmüller. *Phys. Rev. B*, 54:11169, 1996.

[18] G. Kresse and D. Joubert. *Phys. Rev. B*, 59:1758, 1999.

[19] S. Kucherenko. *Application of quasi-Monte Carlo Methods in Global Optimization*, pages 111–133. Springer US, Boston, MA, 2006.

[20] O. Marquardt, L. Geelhaar, and O. Brandt. *Nano Lett.*, 15:4289, 2015.

[21] O. Marquardt, D. Mourad, S. Schulz, T. Hickel, G. Czycholl, and J. Neugebauer. *Phys. Rev. B*, 78:235302, Dec 2008.

[22] O. Marquardt, M. Ramsteiner, P. Corfdir, L. Geelhaar, and O. Brandt. *Phys. Rev. B*, 95:245309, 2017.

[23] M. I. McMahon and R. J. Nelmes. *Phys. Rev. Lett.*, 95:215505, Nov 2005.

[24] H. Niederreiter. *Random Number Generation and quasi-Monte Carlo Methods*. Society for Industrial and Applied Mathematics, 1992.

[25] J. Paier, M. Marsman, K. Hummer, G. Kresse, I. C. Gerber, and J. G. Angyan. *J. Chem. Phys.*, 124:154709, 2006.

[26] J. P. Perdew, M. Ernzerhof, and K. Burke. *J. Chem. Phys.*, 105:9982, 1996.

[27] S. Richard, F. Aniel, and G. Fishman. *Phys. Rev. B*, 70:235204, Dec 2004.

[28] M. M. Rieger and P. Vogl. *Phys. Rev. B*, 48:14276, 1993. See erratum[29].

[29] M. M. Rieger and P. Vogl. *Phys. Rev. B*, 50:8138, 1994.

[30] P. Rinke, M. Winkelnkemper, A. Qteish, D. Bimberg, J. Neugebauer, and M. Scheffler. *Phys. Rev. B*, 77:075202, Feb 2008.

[31] A. Schliwa, M. Winkelnkemper, A. Lochmann, E. Stock, and D. Bimberg. *Phys. Rev. B*, 80:161307, Oct 2009.

[32] I. M. Sobol. *Zh. Vych. Mat. Mat. Fiz.*, 7:784, 1967.

[33] R. G. Veprek, S. Steiger, and B. Witzigmann. *Phys. Rev. B*, 76:165320, Oct 2007.

[34] R. G. Veprek, S. Steiger, and B. Witzigmann. *Journal of Computational Electronics*, 7(4):521–529, Dec 2008.

[35] R. G. Veprek, S. Steiger, and B. Witzigmann. *Optical and Quantum Electronics*, 40(14):1169–1174, Nov 2008.

[36] I. Vurgaftman and J. R. Meyer. *J. Appl. Phys.*, 94:3675, 2003.

[37] I. Vurgaftman, J. R. Meyer, and L. R. Ram-Mohan. *J. Appl. Phys.*, 89:5815, 2001.

[38] S.-H. Wei, S. B. Zhang, and A. Zunger. *Journal of Applied Physics*, 87(3):1304–1311, 2000.

[39] M. Winkelnkemper, A. Schliwa, and D. Bimberg. *Phys. Rev. B*, 74:155322, 2006.

[40] X. Zhou, F. Bertazzi, M. Goano, G. Ghione, and E. Bellotti. *J. Appl. Phys.*, 116:033709, 2014.